



1  
2  
3  
4  
5  
6  
7  
8  
9  
10  
11  
12  
13  
14  
15  
16  
17  
18  
19  
20  
21  
22  
23  
24  
25  
26  
27  
28  
29

**CitcomSVE 3.0: A Three-dimensional Finite Element Software Package for Modeling Load-induced Deformation for an Earth with Viscoelastic and Compressible Mantle**

Tao Yuan<sup>1</sup>, Shijie Zhong<sup>1</sup>, Geruo A<sup>2</sup>

<sup>1</sup>Department of Physics, University of Colorado, Boulder, Colorado, USA  
<sup>2</sup>Department of Earth Sciences, University of California at Irvine, California, USA

E-mail: tao.yuan@colorado.edu



30 **Abstract.** Earth and other terrestrial and icy planetary bodies deform visco-elastically under various forces.  
31 Numerical modeling plays a critical role in understanding the nature of various dynamic deformation  
32 processes. This article introduces a newly developed, open-source package, CitcomSVE-3.0, which  
33 efficiently solves the visco-elastic deformation of planetary bodies. Based on its predecessor, CitcomSVE-  
34 2.1, CitcomSVE-3.0 is updated to account for elastic compressibility and depth-dependent density, which  
35 are particularly important in modeling horizontal displacement for visco-elastic deformation. We  
36 benchmark CitcomSVE-3.0 against a semi-analytical code for two types of surface loading problems: 1)  
37 single harmonic loads on the surface and 2) the glacial isostatic adjustment (GIA) problem with a realistic  
38 ice sheet loading history (ICE-6G\_D), in which an updated version of sea level equations is incorporated.  
39 The benchmark results presented here demonstrate the accuracy and efficiency of this package. CitcomSVE  
40 shows a second-order accuracy in terms of spatial resolution. For a typical GIA modeling with 122-ky  
41 glaciation-deglaciation history, surface horizontal resolution of ~50 km, and time increment of 125 yr, it  
42 takes ~ 3 hours on 384 CPU cores to complete with less than 5% errors in displacement rates.

43



## 44 **1. Introduction**

45 Observations and interpretations of solid Earth's displacement and deformation in response to  
46 surface loadings and tidal forcing are essential in geoscience for at least three important reasons. First,  
47 deglaciation on continents and sea level rise as surface loading processes cause uplifts in glaciated  
48 continental regions and subsidence of sea floor, respectively. The amount of sea level rise during the  
49 deglaciation process critically depends on solid-Earth's response to such surface loading processes  
50 (Mitrovica et al., 2001; Peltier, 1998). Second, the dynamics and stability of ice sheets depend significantly  
51 on the uplift rate of the underlying bedrock as ice sheets melt (Gomez et al., 2018). This process may play  
52 an important role in assessing the fate of West Antarctica ice sheets that have been losing their mass at an  
53 alarming rate. Third, modeling solid-Earth's response to surface loading and comparing the model  
54 predictions with relevant observations (e.g., deglaciation-induced sea level change and crustal  
55 displacements) is the primary way to infer mantle viscosity and rheology (Lambeck et al., 2017; Milne et  
56 al., 2001; Peltier et al., 2015) which is essential to studies of mantle dynamics and Earth's evolution (Zhong  
57 et al., 2007).

58 The solid Earth's response to forcing is determined by solving the equations of motion with relevant  
59 rheological properties of the mantle and crust. Under the assumption of spherical symmetry in elasticity  
60 and viscosity structure (i.e., only 1-D or radial dependence), analytical solutions to the equations of motion  
61 are available in spectral or normal mode domains for the displacement, strain and stress (Longman, 1963;  
62 Takeuchi, 1950; Wu and Peltier, 1982). However, the Earth's mantle structure has significant lateral  
63 variations as demonstrated by seismic imaging studies on both global (Ritsema et al., 2011; French and  
64 Romanowicz, 2015; Tromp, 2020) and regional (e.g., Lloyd et al., 2020) scales. Because of the large  
65 sensitivity of mantle viscosity to temperature, lateral variations in mantle viscosity are expected to exceed  
66 several orders of magnitude (e.g., Paulson et al., 2005; Ivins et al., 2023). For the mantle with fully 3-D  
67 elastic and viscosity structures, numerical solution methods are required to solve the equations of motion.  
68 The necessity for numerical solution methods has become increasingly more evident as more observations



69 of higher quality (e.g., Bevis et al., 2012) become available to place constraints on the models. In recent  
70 years, numerous numerical methods have been developed, including a spectral-finite element (Martinec,  
71 2000; Klemann et al., 2008; Bagge et al., 2021), finite element (Zhong et al., 2003, 2022; A et al., 2013;  
72 Paulson et al., 2005), finite volume (Latychev et al., 2005), and coupled spectral-finite element (Wu, 2004;  
73 Van Der Wal et al., 2013; Huang et al., 2023) methods.

74 The CitcomSVE package is a finite element modeling package for solving load-induced  
75 viscoelastic deformation problems in a 3-D spherical shell, a spherical wedge or a Cartesian domain.  
76 CitcomSVE solves the sea level equation and incorporates the effects of polar wander and apparent motion  
77 of the center of the mass (Zhong et al., 2003, 2022; A et al., 2013; Paulson et al., 2005). CitcomSVE works  
78 for 3-D viscoelastic mantle structures with either linear or non-linear viscosity. It works efficiently on  
79 massively parallel computers (>6,000 CPU cores), making it feasible for routine high-resolution GIA  
80 modeling calculations (~30 km horizontal resolution on the Earth's surface and ~10 km vertical resolution  
81 in the upper mantle). CitcomSVE, developed over the last two decades, has been used in GIA studies for  
82 both the incompressible (Zhong et al., 2003, 2022) and compressible (A et al., 2013) mantle with  
83 temperature- (Paulson et al., 2005) and stress-dependent viscosity (Kang et al., 2022), and in tidal  
84 deformation studies for the Moon (Zhong et al., 2012; Qin et al., 2014; Fienga et al., 2024). CitcomSVE  
85 was built from the mantle convection modeling package CitcomS (Zhong et al., 2000, 2008) by replacing  
86 viscous rheology and Eulerian formulation in CitcomS with viscoelastic rheology and Lagrangian  
87 formulation, respectively (Zhong et al., 2003, 2022).

88 Recently, Zhong et al. (2022) presented an expansive set of benchmark calculations for single  
89 harmonic surface loading, tidal loading, and glaciation and deglaciation loading history (i.e., ICE-6G) for  
90 a significantly improved version of CitcomSVE 2.1. Compared with previous versions of CitcomSVE that  
91 only used 12 CPU cores (e.g., Zhong et al., 2003; A et al., 2013), the most important improvement with  
92 CitcomSVE 2.1 is its capability of efficiently using any large number of CPU cores (e.g., > 6000 CPU cores  
93 as in Zhong et al., (2022)). CitcomSVE 2.1 has also become the first GIA modeling software package that



94 is open source and publicly available via GitHub (Zhong et al., 2022). However, CitcomSVE 2.1 is for an  
95 incompressible mantle, which limits its applications, especially for studies on GIA-induced horizontal  
96 crustal motions and where realistic elastic structure (e.g., PREM) is necessary (Mitrovica et al., 1994).

97 This paper presents CitcomSVE 3.0, an extension of CitcomSVE 2.1, by incorporating mantle  
98 compressibility as in A et al. (2013). While the numerical techniques for implementing mantle  
99 compressibility are the same as in A et al. (2013), this paper includes significantly more detailed benchmark  
100 calculations and an improved sea level equation solver. With its public availability via GitHub and efficient  
101 parallel computing, CitcomSVE 3.0 offers the scientific community a powerful computational tool for  
102 solving an important class of geodynamic questions, including the GIA and tidal deformation for Earth's  
103 mantle with realistic viscosity and rheology. The paper is organized as follows. The next section describes  
104 the governing equations for dynamic loading problems and numerical methods. Section 3 defines  
105 benchmark problems and presents benchmark results, including error analyses. Discussions and  
106 conclusions are given in the final section.

## 107 **2. Governing Equations and Numerical Methods**

### 108 **2.1. Governing Equations and Viscoelastic Properties of the Mantle**

109 The governing equations for load-induced deformation are derived from the conservation laws of  
110 mass and momentum and Newton's law of gravitation, together with viscoelastic constitutive equation (Wu  
111 and Peltier, 1982; A et al., 2013):

$$112 \quad \rho_1^E = -(\rho_0 u_i)_{,i}, \quad (1)$$

$$113 \quad \sigma_{ij,j} + \rho_0 \phi_{,i} - (\rho_0 g u_r)_{,i} - \rho_1^E g_i + \rho_0 V_{a,i} = 0, \quad (2)$$

$$114 \quad \phi_{,ii} = -4\pi G \rho_1^E, \quad (3)$$

115 where  $\rho_1^E$  is the Eulerian density perturbation,  $\rho_0$  is the unperturbed mantle density,  $u_i$  represents the  
116 displacement vector with  $u_r$  being in the radial direction,  $\sigma_{ij}$  is the stress tensor,  $\phi$  is the perturbation of



117 gravitational potential due to deformation,  $V_a$  is the applied potential (e.g., rotational and tidal potentials)  
118 when applicable,  $g_i$  is the gravitational acceleration with  $g = \sqrt{g_i g_i}$ , and  $G$  is the gravitational constant.  
119 The equations are written in an indicial notation such that  $A_{,i}$  represents the derivative of variable  $A$  with  
120 respect to coordinate  $x_i$ , and repeated indices indicate summation.

121 Both the surface (at radius  $r = r_s$ ) and core-mantle boundary (CMB) ( $r = r_b$ ) experience zero  
122 shear force but are subjected to normal forces

$$123 \quad \sigma_{ij} n_j = -\sigma_o n_i, \quad \text{for } r = r_s, \quad (4)$$

$$124 \quad \sigma_{ij} n_j = (-\rho_c \phi + \rho_c g u_r) n_i, \quad \text{for } r = r_b, \quad (5)$$

125 where  $\sigma_o$  represents the pressure loads at the surface (e.g., glacial loads) as a function of time and space,  
126  $\rho_c$  is the density of the core, and  $n_i$  represents the normal vector of the surface or CMB. The boundary  
127 conditions at the CMB consider the self-gravitational effect for a fluid core (e.g., Zhong et al., 2003). Except  
128 for this CMB boundary condition, the core is not considered explicitly in our numerical formulation. With  
129 such boundary conditions of forces, both the surface and CMB can deform dynamically in both horizontal  
130 and radial directions.

131 CitcomSVE has implemented formulations for both incompressible (e.g., Zhong et al., 2003; 2022)  
132 and compressible (A et al., 2013) medium. In this study for compressible medium, we follow the  
133 formulation by A et al., (2013). Here, we will only provide a general description for the formulation and  
134 numerical analyses. The details for the compressibility-related topics and numerical analyses of CitcomSVE  
135 can be found in A et al., (2013) and Zhong et al., (2022), respectively. Note that CitcomSVE also  
136 incorporates the effects of polar wander and apparent motion of the center of mass (i.e., degree-1  
137 deformation), and uses a reference frame centered at the center of mass including the mass of loads with no  
138 net rotation of the mantle and crust (Zhong et al., 2022; Paulson et al., 2005; A et al., 2013).



139 The Earth's mantle is considered as a compressible Maxwell solid, and the constitutive equation  
140 can be written as (e.g., Wu and Peltier, 1982)

$$141 \quad \dot{\sigma}_{ij} + \frac{\mu}{\eta} (\sigma_{ij} - \frac{1}{3} \sigma_{kk} \delta_{ij}) = \lambda \dot{\epsilon}_{kk} \delta_{ij} + 2\mu \dot{\epsilon}_{ij}, \quad (6)$$

142 where  $\eta$  is the viscosity,  $\lambda$  and  $\mu$  are the Lamé parameters, and  $\delta_{ij}$  is the Kronecker delta function. The  
143 strain  $\epsilon_{ij}$  is related to the displacement by  $\epsilon_{ij} = \frac{1}{2}(u_{i,j} + u_{j,i})$ . Both Lamé parameters ( $\lambda$  and  $\mu$ ) and  
144 viscosity  $\eta$  can be fully 3-dimensional in CitcomSVE models to represent the effects of temperature,  
145 composition and stress on mantle mechanical properties (e.g., Zhong et al., 2003; A et al., 2013; Kang et  
146 al., 2022). However, for this benchmark study, we will only consider radially layered  $\lambda$ ,  $\mu$ , and  $\eta$ .

## 147 2.2. Numerical Analysis

148 A finite element method is employed in CitcomSVE to solve the governing equations (1)-(3) for  
149 load-induced displacement under boundary conditions (4)-(5) with a Maxwell rheological equation (6)  
150 (Zhong et al., 2003; 2022; A et al., 2013). However, before presenting a weak form of the governing  
151 equations for the finite element analysis, it is necessary to introduce an incremental displacement  
152 formulation, re-formulate the time-dependent rheological equation (i.e., equation 6), and discuss solution  
153 strategies for the gravitational potential that results from mass anomalies associated with mantle  
154 deformation via the Eulerian density perturbation  $\rho_1^E$  as controlled by the Poisson's equation (i.e., equation  
155 3).

156 Define  $u_i^n$  and  $u_i^{n-1}$  as displacements at times  $t$  and  $t-\Delta t$ , respectively, where superscripts  $n$  and  $n-$   
157  $l$  represent time steps. Incremental displacement at time  $t$ ,  $v_i^n$ , is defined as  $v_i^n = u_i^n - u_i^{n-1}$  and it is  
158 related to incremental strain  $\Delta \epsilon_{ij}^n$  as

$$159 \quad \Delta \epsilon_{ij}^n = \frac{1}{2} (v_{i,j}^n + v_{j,i}^n). \quad (7)$$



160 Rheological equation (6) is discretized in time by integrating it from time  $t-\Delta t$  to  $t$ , and stress tensor at time  
 161  $t$ ,  $\sigma_{ij}^n$ , is given in terms of incremental strain  $\Delta\varepsilon_{ij}^n$ , stresses at time step  $n-1$  (i.e., pre-stress), and material  
 162 properties as (A et al., 2013; Zhong et al., 2003),

$$163 \quad \sigma_{ij}^n = \tilde{\lambda}\Delta\varepsilon_{kk}^n\delta_{ij} + 2\tilde{\mu}\Delta\varepsilon_{ij}^n + \tau_{ij}^{pre}, \quad (8)$$

164 where  $\tau_{ij}^{pre} = (1 - \frac{\Delta t}{2\alpha})/(1 + \frac{\Delta t}{2\alpha})\sigma_{ij}^{n-1} + \frac{\Delta t}{3\alpha}/(1 + \frac{\Delta t}{2\alpha})\sigma_{kk}^{n-1}\delta_{ij}$ ,  $\tilde{\lambda} = [\lambda + (\lambda + \frac{2\mu}{3})\frac{\Delta t}{2\alpha}]/(1 + \frac{\Delta t}{2\alpha})$ ,  
 165  $\tilde{\mu} = \mu/(1 + \frac{\Delta t}{2\alpha})$ ,  $\alpha = \eta/\mu$  is the Maxwell time, and  $\tau_{ij}^{pre}$  represents the pre-stress at timestep  $n-1$  (A et al.,  
 166 2013).

167 The Poisson's equation for gravitational potential anomaly  $\phi$  (i.e., equation 3) is solved in a  
 168 spherical harmonic domain for mass anomalies associated with the Eulerian density perturbation  $\rho_1^E$  and  
 169 the loads (e.g., ice and water loads). For a compressible mantle,  $\rho_1^E$  exists throughout the mantle and crust  
 170 (see equation 1), and it is necessary to express  $\rho_1^E$  at each depth in terms of spherical harmonic degree  $l$  and  
 171 order  $m$ . The gravitational potential anomaly at radius  $r$  and time  $t$  and at degree  $l$  and order  $m$ ,  $\phi_{lm}(r, t)$ ,  
 172 can be related to mass anomalies via Green's function formulation (e.g., A et al., 2013; Zhong et al., 2008).  
 173 The solution of  $\phi_{lm}(r, t)$  needs to recast to finite element grid points in solving the equation of motion  
 174 (i.e., equation 2). It should be pointed out that the transformation for gravitational potential anomalies  $\phi$   
 175 between the spherical harmonic domain and the spatial domain is computationally rather expensive.

176 We now present the weak form of the equation of motion (i.e., equation 2) for the compressible  
 177 mantle as (A et al., 2013)

$$178 \quad \int_{\Omega} w_{i,j} [\tilde{\lambda}v_{k,k}\delta_{ij} + \tilde{\mu}(v_{i,j} + v_{j,i})] dV - \int_{\Omega} \rho_0 g(w_{i,i}v_r + w_r v_{i,i}) dV + \sum_l \int_S w_r \Delta\rho_l g v_r dS_l$$

$$179 \quad = - \int_{\Omega} w_{i,j} \tau_{ij}^{pre} dV + \int_{\Omega} \rho_0 g(w_{i,i}U_r + w_r U_{i,i}) dV - \int_{\Omega} w_{i,i} \rho_0 \phi dV$$

$$180 \quad + \sum_l \int_{S_l} w_r (\Delta\rho_l \phi - \Delta\rho_l g U_r + \rho_0 V_a) dS_l - \int_S w_r \sigma_0 dS, \quad (9)$$





181 where integration domain  $\Omega$ ,  $S_i$ , and  $S$  are for the volume, the horizontal surface at some depth with the  $l$ -th  
182 density boundary, and the Earth's surface, respectively,  $w_i$  is the displacement weighting function,  $U_i$  is the  
183 cumulative displacements at the previous time step,  $V_a$ , the applied potential, is only relevant for tidal  
184 loading problems, and  $\sigma_0$  is the surface load. Note that the gravitational potential anomalies  $\phi$  in equation  
185 (9) depend on unknown incremental displacement  $v_i$ . We decompose  $\phi$  into  $\phi = \Phi + \Delta\phi(v_i)$ , where  $\Phi$  is  
186 the total potential at the previous time step and  $\Delta\phi(v_i)$  is the incremental potential determined by  $v_i$  and  
187 other incremental mass anomalies at the current time step.

188 Equation (9) is discretized onto a set of finite element grids to form a system of matrix equations  
189 with unknown vectors of incremental displacement  $\{V\}$ .

$$190 \quad [K]\{V\} = \{F_0\} + \{F(\Delta\phi)\}, \quad (10)$$

191 where  $[K]$  is the stiffness matrix,  $\{F_0\}$  is the force vector representing contributions from the previous time  
192 step, and  $\{F(\Delta\phi)\}$  represents contributions from the incremental potential  $\Delta\phi$  which depends on the  
193 unknown displacement  $\{V\}$  and other incremental mass anomalies. An iteration scheme is applied to  
194 equation (10) to obtain a convergent solution for  $\{V\}$  (Zhong et al., 2003).

195 CitcomSVE was derived from the 3-D finite element code CitcomS for mantle convection in a  
196 spherical shell, and they share many common features including the grid. The spherical shell of the mantle  
197 is divided into 12 caps of similar size, and each cap is further divided into a grid of cells (i.e., elements) of  
198 similar size with eight displacement nodes per element (Zhong et al., 2000; 2008; 2022). This design of  
199 finite element grid is suited for parallel computing, as discussed in Zhong et al., (2008). An important  
200 feature of this grid is its approximately uniform resolution from the polar to equatorial regions (Zhong et  
201 al., 2000; 2003), different from the spectral finite element GIA codes (e.g., Martinec, 2000; Klemann et al.,  
202 2008; Wu, 2004; van der Wal et al., 2013; Huang et al., 2023).



203 Matrix equation (10) is solved with a parallelized full multigrid method (Zhong et al., 2000; 2008).  
204 The general solution strategy in CitcomSVE follows an iterative scheme that can be summarized as (Zhong  
205 et al., 2003; A et al., 2013):

- 206 1) At a given time  $t$ ,  $\{F_0\}$  is first evaluated using pre-stress  $\tau_{ij}^{pre}$ , gravitational potential  $\Phi$  and  
207 displacements  $U_i$  at the previous time step,  $t-\Delta t$ , and set  $\{F\} = \{0\}$ .
- 208 2) Solve equation (10) using the full multigrid method for incremental displacements  $\{V\}$ , using  $\{F_0\}$   
209 and  $\{F\}$ .
- 210 3) Compute incremental potential  $\Delta\phi_{lm}(r, t)$  by solving equation (3) with the incremental  
211 displacements from step 2, and then re-evaluate  $\{F\}$ . Go back to step 2 to solve for  $\{V\}$  again.
- 212 4) Repeat steps 2 and 3, until  $\{V\}$  converges to a given threshold error tolerance. Then go back to step  
213 1 to march forward in time.

214 In the implementation of equation (10) in CitcomSVE, all the variables and parameters are  
215 normalized to be dimensionless, and the outputs are also dimensionless. CitcomSVE uses the following  
216 normalization scheme. The coordinates  $x_i$  and displacements  $u_i$  and  $v_i$  are all normalized by the radius of  
217 a planet,  $r_s$ . The time is normalized by a reference mantle Maxwell time  $\alpha = \eta_r / \mu_r$ , where  $\eta_r$  and  $\mu_r$  are  
218 the reference mantle viscosity and shear modulus, respectively.  $\eta_r$  is also used to normalize mantle  
219 viscosity and  $\mu_r$  is used to normalize elastic moduli, stress tensor and pressure, while the density is  
220 normalized by reference density  $\rho_0$ . Gravitational potential and centrifugal potential are normalized by  
221  $4\pi G\rho_0 r_s^2$ , and the geoid anomalies are normalized by  $4\pi G\rho_0 r_s^2 / g$ . Any other variables can be normalized  
222 by combining the abovementioned scales. However, model input parameters are defined by users as  
223 dimensional values. For example, 3-D mantle viscosity and elasticity models are given by users in separated  
224 files on a regular grid (e.g.,  $1^\circ \times 1^\circ$  grid) at different depths. CitcomSVE reads these parameters from the  
225 files, normalizes them, and interpolates them onto the finite element grids. Along with public releases of  
226 CitcomSVE 2.1 and 3.0 on GitHub, a user manual is available to describe the usage of the code and the  
227 input and output files.



228           We now finish this section by highlighting the two main differences between incompressible and  
229 compressible models in CitcomSVE (i.e., versions 2.1 versus 3.0). First, the compressible model presented  
230 here does not include the pressure term which is a key component of incompressible models. The absence  
231 of the pressure term simplifies the matrix equation (i.e., equation 10) and its solution procedure, but for the  
232 incompressible model, a two-level Uzawa algorithm is needed to solve for both the pressure and  
233 displacement. Second, mantle compressibility causes mass anomalies or Eulerian density perturbation  $\rho_1^E$   
234 throughout the mantle, while for an incompressible mantle, mass anomalies only exist at the surface and  
235 CMB. Consequently, the compressible model is computationally more expensive, particularly for  
236 calculating the gravitational potential anomalies.

### 237   2.3. Sea Level Change and Sea Level Equation

238           Understanding and modeling sea level change is important for GIA studies. Sea level change is  
239 controlled by ice volume change and GIA-induced vertical crustal motion and gravitational potential  
240 change. Therefore, the records of sea level change provide essential constraints on GIA processes, including  
241 ice volume change and mantle viscosity. Moreover, sea level change acts as a change of load on the surface,  
242 affecting solid-Earth deformation and gravitational potential. Modeling the GIA processes, one of the major  
243 applications of the CitcomSVE package, requires an accurate sea level equation that describes the sea level  
244 change in this process. A major improvement of CitcomSVE 3.0 over its previous versions is on modeling  
245 sea level changes, and a detailed description is given in this section.

246           The original sea level equation formulated by Farrell and Clark (1976) provides an elegant way to  
247 incorporate the sea level change into GIA models and can explain the diverging pattern of sea level change  
248 in different regions (e.g., near or far away from former ice sheets). However, the simplified formulation by  
249 Farrell and Clark ignored several factors affecting the accuracy of sea level change modeling. One key  
250 simplification is on the time-dependent ocean-continent function that describes the ocean and continent  
251 distribution, which was assumed to be constant through time in their formulation. The ocean area has varied  
252 by several percent since the last glacial maximum because of the shoreline evolution induced by sea level



253 rise or fall (Fig. S1). Accounting for the time-dependent ocean-continent function requires modifications  
254 of the sea level equation and affects the predicted sea level change by tens of meters for some regions  
255 compared to that based on Farrell and Clark's formulation (Kendall et al., 2005). Kendall et al. (2005)  
256 provides a modified sea level equation that accounts for the time-dependent ocean function, in which the  
257 variation of ocean area is mainly attributed to two factors: 1) formation or melting of marine ice sheets (i.e.,  
258 ice sheets that lie below sea level), 2) the evolution of shorelines related to the sloping bathymetry and local  
259 sea level change. In previous versions of CitcomSVE, we only considered the variation of ocean function  
260 related to marine ice sheets (A et al., 2013; Zhong et al., 2022). In our new formulation, the sea level  
261 equation is modified to follow the formulation of Kendall et al. (2005). The new sea level equation can be  
262 summarized as follows:

$$263 \quad L_0(\theta, \phi, t) = [N(\theta, \phi, t) - U(\theta, \phi, t) + c(t)]O(\theta, \phi, t) \\ 264 \quad - T_0(\theta, \phi)[O(\theta, \phi, t) - O(\theta, \phi, t_0)], \quad (11)$$

265 Where  $t$  is the time with  $t_0$  as the initial time (i.e., the onset of loading),  $\theta$  and  $\phi$  are co-latitude and  
266 longitude, respectively,  $L_0$  is the change in sea level relative to the initial stage,  $N$  and  $U$  are GIA-induced  
267 geoid anomalies and surface radial displacement,  $O$  is ocean function (1 for ocean and 0 elsewhere),  $T_0$  is  
268 initial topography at  $t_0$ , and  $c$  is introduced for the conservation of water mass and is defined as:

$$269 \quad c(t) = \frac{1}{A_0(t)} \left\{ -\frac{M_{ice}(t)}{\rho_w} - \int [N(\theta, \phi, t) - U(\theta, \phi, t)]O(\theta, \phi, t)dS \right. \\ 270 \quad \left. + \int T_0(\theta, \phi)[O(\theta, \phi, t) - O(\theta, \phi, t_0)]dS \right\}, \quad (12)$$

271 where  $M_{ice}$  is the ice mass change relative to the initial stage (i.e.,  $t_0$ ),  $A_0$  is the ocean area at time  $t$ ,  $\rho_w$  is  
272 water density,  $N$  and  $U$  are relative to  $t_0$ , and the integral is for the surface of Earth. Following Kendall et  
273 al. (2005), a check for grounded ice is incorporated using the criterion that at any location with  
274 topography  $T$  and ice of thickness  $I$  and of density  $\rho_i$ , the ice is considered as ground ice if  $I\rho_i > -T\rho_w$ .  
275 Only grounded ice is treated as ice load, whereas regions with non-grounded ice (i.e., floating ice) are



276 treated as oceans. Note that regions with topography  $T < 0$  and without grounded ice are considered as  
277 ocean where the ocean surface follows the geoid.

278         The sea level equation can only be solved iteratively because the ocean load associated with sea  
279 level change and ocean function  $O(t)$  affect each other, and the unknown initial topography  $T_0$  needs to be  
280 determined iteratively to keep the modeled present-day topography consistent with the observed present-  
281 day topography. The algorithm for solving the sea level equation in Kendall et al., (2005) adds an outer  
282 layer of iterations to an otherwise normal GIA modeling that uses pre-determined initial topography  $T_0$  and  
283 time-dependent ocean function  $O(t)$  to determine  $N(t)$ ,  $U(t)$ , and  $L_0(t)$  for each time  $t$  from  $t_0$  to the  
284 present day. In the outer layer iteration calculations, at the end of each single complete GIA model run,  
285 time-dependent ocean function  $O(t)$  and paleo-topography including initial topography  $T_0$  are updated  
286 using newly calculated  $U(t)$  and  $N(t)$  and the present-day topography, and the updated  $T_0$  and  $O(t)$  are  
287 then used for next GIA model run. The iteration procedure continues until the initial topography converges.  
288 In practice, the model results would not be altered significantly beyond the second outer iteration. However,  
289 there are noticeable differences in results (e.g., modeled RSL histories) between the first and second outer  
290 iterations for some sites following the algorithm developed by Kendall et al. (2005).

291         We implemented the algorithm developed by Kendall et al. (2005) in our semi-analytic code (e.g.,  
292 A et al., 2013) and produced consistent results with Kendall et al. (2005). However, running two or three  
293 outer iterations where each iteration is a complete GIA model run of a glacial cycle is computationally  
294 expensive, especially for numerical modeling such as in CitcomSVE, and it would be more efficient if the  
295 results from the first outer iteration (i.e., a single complete GIA model run) can be sufficiently accurate. In  
296 Kendall's algorithm, the time-dependent ocean function  $O(t)$  for the first outer iteration is constructed  
297 using fixed shorelines same as that of the present day, except that the extent of oceans may be limited by  
298 the existence of grounded marine ice sheets. However, we found that the first iteration may produce much  
299 improved solutions if  $O(t)$  for the first outer iteration is constructed by calculating the change of ocean area  
300 (i.e., ocean-continent transitions) based on ice volume change (i.e.,  $M_{ice}$ ) and the present-day topography



301 (bathymetry), assuming barostatic sea level change on a rigid Earth (i.e., no radial surface displacement).  
302 The ocean function generated in this way generally captures the shoreline evolution for regions experienced  
303 ocean-land transition, and this approximation makes it easy to derive the time-dependent ocean function  
304 for any given ice model. In the next section, we will show the effectiveness of this single outer iteration  
305 method using the improved ocean function in both our semi-analytic solution method and CitcomSVE 3.0.

### 306 **3. Example Calculations and Benchmark Results**

307 Two example problems solved using CitcomSVE 3.0 are presented here. They are: 1) surface  
308 loading problems with a single spherical harmonic in space and step-function (i.e., Heaviside function) in  
309 time; 2) GIA problems with ICE-6G\_D ice history model. For each example problem, the elastic and  
310 viscosity structures are chosen to be dependent only on the radius (i.e., 1-D) so that CitcomSVE solutions  
311 can be benchmarked against semi-analytical solutions. The following benchmarks largely follow the  
312 approaches of Zhong et al. (2022).

#### 313 **3.1. Surface loading in a single spherical harmonic in space and step-function in time.**

314 3.1.1. Definition of the surface loading problem.

315 For the first example problem, we consider a surface load  $\sigma_0$  (see equation 4) corresponding to  
316 amplitude of topographic variation  $d$  with density  $\rho_0$  at a single harmonic function in space and step-  
317 function in time:

$$318 \quad \sigma_0(t, \theta, \varphi) = \rho_0 g d \cos(m\varphi) p_{lm}(\theta) H(t) = \rho_0 g d \bar{P}_{lm}(\theta, \varphi) H(t), \quad (13)$$

319 where  $H(t)$  is the Heaviside function (i.e.,  $H(t)=1$  for  $t \geq 0$ ;  $H(t)=0$  otherwise) and  $\bar{P}_{lm}(\theta, \varphi) =$   
320  $\cos(m\varphi) p_{lm}(\theta)$  is the cosine part of spherical harmonic functions in the real form. Note that only cosine  
321 terms of longitudinal dependence are considered for simplicity. A small amplitude of the load height is used  
322 to avoid large grid deformations. We assume an ocean-free Earth for this example and ignore any sea-level-  
323 related calculations. The density and Lamé parameters for lithosphere and mantle are from PREM, except  
324 that for the crust layer those properties are replaced to be same as the underlying mantle, and the viscosity



325 structure is from VM5a (Peltier et al, 2015). See Table 1 for model parameters. Time-dependent surface 3-  
 326 D displacements and gravitational potential anomalies are computed using the newly updated CitcomSVE  
 327 and compared with those from semi-analytical solutions (Han and Wahr, 1995; Paulson et al., 2005; A et  
 328 al., 2013). The results are presented in terms of load Love numbers  $h_l$ ,  $k_l$ , and  $l_l$  at harmonic degree  $l$  for  
 329 radial displacement, gravitational potential, and horizontal displacement, respectively. The definitions of  
 330 load Love numbers in the context of CitcomSVE calculations are given in equations 37-41 of Zhong et al.,  
 331 (2022).

**Table 1. Model parameters for benchmarks**

Model parameters	value
Earth radius $r_s$	6371 km
CMB radius $r_b$	3485.5 km
Reference density $\rho_0$	4400 kg/m <sup>3</sup>
Core density	10895.62 kg/m <sup>3</sup>
Water density $\rho_w$	1000 kg/m <sup>3</sup>
Ice density $\rho_i$	917.4 kg/m <sup>3</sup>
Reference shear modulus $\mu$	1.4305x10 <sup>11</sup> Pa
Modified Fluid Love number $k_{2l}(1+\delta)$	0.9521091
Mantle reference viscosity $\eta$	2x10 <sup>21</sup> Pa·s
Gravitational acceleration $g$	9.82 m·s <sup>-2</sup>
VM5A viscosity model:	
The surface to 60 km depth	10 <sup>26</sup> Pas
60 to 100 km depth	10 <sup>22</sup> Pas
100 to 670 km depth	4.853x10 <sup>21</sup> Pas
670 to 1170 km	1.5048x10 <sup>21</sup> Pas
1170 km to CMB	3.095x10 <sup>21</sup> Pas

332

333



334 3.1.2. Benchmark results.

335 We have computed a set of model cases using CitcomSVE for four numerical resolutions and six  
 336 loading harmonics. Four different numerical resolutions of R1-R4 are for 12x(32x32x32), 12x(64x64x64),  
 337 12x(64x96x96) and 12x(64x128x128), respectively, where the first number, 12, indicates the number of  
 338 spherical caps that the spherical surface is divided into, and the subsequent numbers indicate the number of  
 339 elements in the radial and two horizontal directions in each cap (Zhong et al., 2022). Six different loading  
 340 harmonics are included for (1,0), (2, 0), (2,1), (4, 0), (8, 4), and (16, 8) where the first and second numbers  
 341 in parenthesis ( $l, m$ ) indicate spherical harmonic degree  $l$  and order  $m$ , respectively. Each case is named by  
 342 its loading harmonic and numerical resolution; for example, case l2m0\_R1 corresponds to the case where  
 343 the loading harmonic is (2, 0) and the resolution is R1. For l16m8, an additional case with resolution  
 344 12x(80x128x128) is included (i.e., l16m8\_R5). Each case is computed for 40 Maxwell times (i.e.,  $40\alpha$  or  
 345 non-dimensional time of 40), using a non-dimensional time increment of 0.2. Figure 1 shows  $h_l(t)$ ,  $k_l(t)$ ,  
 346 and  $|l_l(t)|$  for cases with different loading harmonics and numerical resolutions, together with semi-  
 347 analytical solutions. Table 2 shows both numerical and analytical results of these Love numbers at  $t=0$  and  
 348 40 for a selected set of cases (supplementary Table S1 for all the cases). Solutions at  $t=0$  represent the  
 349 elastic responses of Earth, and the magnitudes of those Love numbers generally increase with time due to  
 350 viscous relaxation and finally reach nearly stable states after certain time periods (Fig. 1).

351

352 **Table 2: Comparison of Load Love Numbers  $h_l$ ,  $k_l$ , and  $l_l$  Between CitcomSVE and Semi-Analytical**  
 353 **Solutions**

Case <sup>a</sup>	$h_l(0)^b$	$k_l(0)$	$ l_l(0) $	$h_l(40)$	$k_l(40)$	$ l_l(40) $
<b>11m0</b>	-1.2546(-1.2543)	-1.0000(-1.0000)	0.8864(0.8866)	-1.4968(-1.4964)	-1.0000(-1.0000)	1.9101(1.9090)
<b>12m0</b>	-0.9574(-0.9577)	-0.3038(-0.3041)	0.0203(0.0200)	-2.4066(-2.4066)	-0.9392(-0.9396)	0.8229(0.8216)
<b>12m1</b>	-0.3056(-0.3058)	1.0948(1.0944)	0.1118(0.1118)	0.6178(0.6151)	2.2003(2.1973)	0.1891(0.1884)
<b>14m0</b>	-1.0247(-1.0251)	-0.1341(-0.1342)	0.0569(0.0568)	-4.4395(-4.4402)	-0.9410(-0.9416)	0.3423(0.3411)
<b>18m4</b>	-1.2372(-1.2376)	-0.0772(-0.0772)	0.0303(0.0302)	-8.8084(-8.8405)	-0.9563(-0.9605)	0.0977(0.0958)
<b>116m8</b>	-1.6825(-1.6868)	-0.0573(-0.0574)	0.0228(0.0229)	-17.535(-17.847)	-0.9530(-0.9726)	0.0435(0.0479)
<b>116m8_R5</b>	-1.6805(-1.6868)	-0.0572(-0.0574)	0.0228(0.0229)	-17.623(-17.847)	-0.9579(-0.9726)	0.0464(0.0479)

354

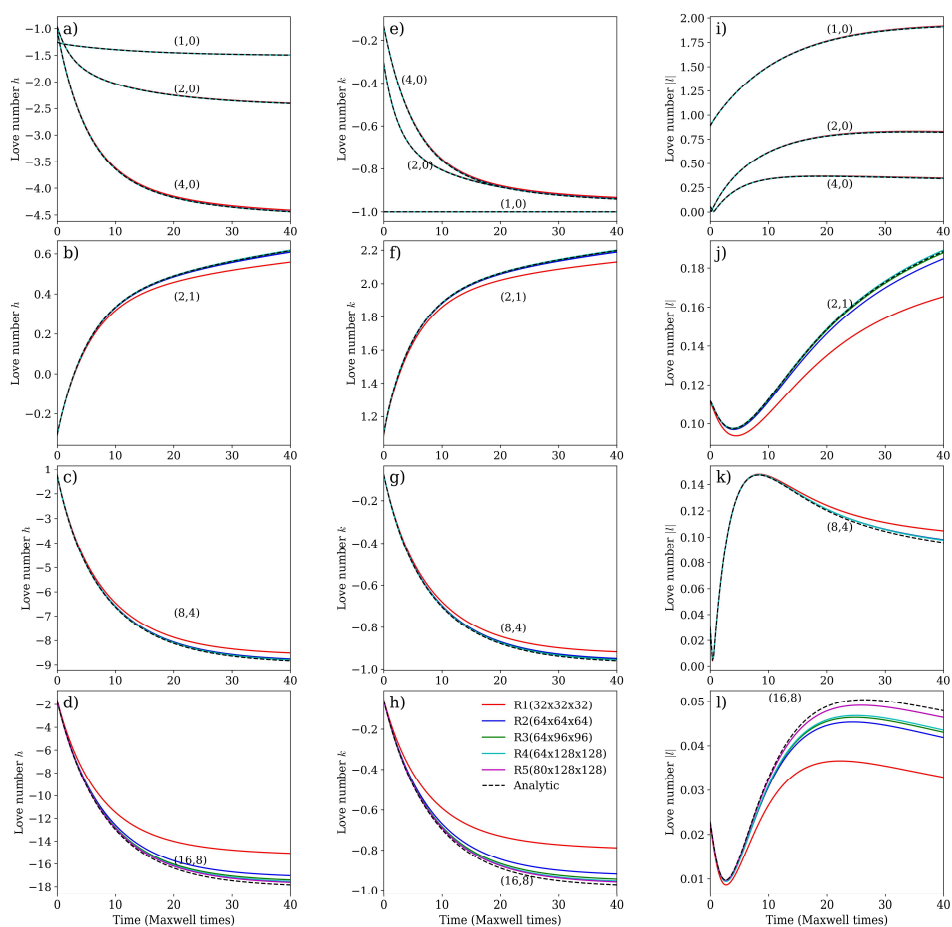




355 <sup>a</sup>Case names follow this notation:  $l1m0$  stands for loading harmonic for  $l=1$  and  $m=0$ . All CitcomSVE  
 356 solutions in this table are for resolution R4 ( $12 \times 64 \times 128 \times 128$ ), except for  $l16m8\_R5$ , which has a resolution  
 357 R5 ( $12 \times 80 \times 128 \times 128$ ).

358 <sup>b</sup>Load Love numbers are provided at 0 and 40 Maxwell time. Each entry includes semi-analytical solutions  
 359 inside the parentheses and CitcomSVE solutions outside the parentheses.

360



361

362 Figure 1. Love numbers  $h$ ,  $k$  and  $l$  for cases with different loading harmonics from CitcomSVE and  
 363 analytical solutions. The first, second, and third columns are for Love number  $h$ ,  $k$  and  $|l|$  (i.e., the absolute  
 364 values of Love number  $l$ ), respectively. The first row is for loading harmonics (1,0), (2,0) and (4,0). The  
 365 following rows are for loading harmonics (2,1), (8,4) and (16,8), respectively. Each loading case has  
 366 solutions from four different spatial resolutions (R1-R4), except that loading case (16,8) has an additional  
 367 calculation with resolution R5.



368 The comparison shows a good agreement between numerical solutions and semi-analytical  
369 solutions. For long-wavelength loadings (e.g., 11m0, 12m0, and 14m0), numerical solutions at different  
370 resolutions (R1-R4) are nearly identical to semi-analytical solutions, as shown in Figure 1. However, for  
371 12m1 cases with the polar wander effect, resolution R1 shows significant numerical errors, whereas  
372 calculations with higher resolutions (R2-R4) deliver a remarkable fit to the semi-analytical solution,  
373 suggesting that polar wander is more challenging to compute in numerical models (e.g., Paulson et al., 2005;  
374 A et al., 2013; Zhong et al., 2022). For shorter wavelengths (such as 18m4 and 116m8), low-resolution  
375 numerical results differ noticeably from semi-analytical solutions. As the numerical resolution increases,  
376 the results match the semi-analytical solutions much more closely (Figure 1). For 116m8, case R5  
377 significantly reduces errors in  $l_l$  compared to R4. Note that R5 has a higher vertical resolution in the upper  
378 mantle but the same horizontal resolution as R4 (Fig.1 and Table 2). Grid size in the vertical direction is  
379 not uniform since grids get refined vertically in the upper mantle and lithosphere for each model. For cases  
380 with 64 elements in the vertical direction (R2, R3 and R4), the vertical resolutions are about 20 km, 40 km,  
381 and more than 50 km in the lithosphere, upper mantle and lower mantle, respectively, whereas R5, with a  
382 total of 80 elements in the vertical direction, has a vertical resolution  $\sim 20$  km in the upper mantle. Note  
383 that the load Love number for horizontal displacement is presented as  $|l_l(t)|$ , because CitcomSVE only  
384 conveniently determines  $l_l^2(t)$  (Zhong et al., 2022), although it is possible to determine the  $l_l$  based on  
385 vector spherical harmonic decomposition of horizontal surface motion (Wu and Peltier 1982).

386 We determine numerical errors by computing amplitude and dispersion errors (e.g., Zhong et al.,  
387 2003; A et al., 2013; Zhong et al., 2022). Amplitude error  $\varepsilon_a$  and dispersion error  $\varepsilon_d$  are computed using  
388 the following equations (Zhong et al., 2022):

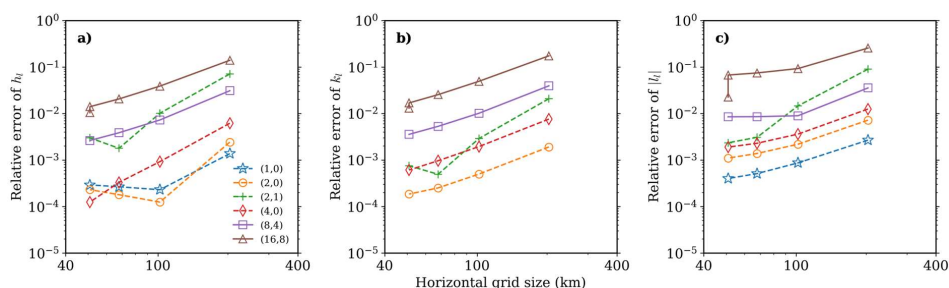
389 
$$\varepsilon_a = \frac{\int_0^T |S_n(l_0, m_0, t) - S_{sa}(l_0, m_0, t)| dt}{\int_0^T |S_{sa}(l_0, m_0, t)| dt}, \quad (14)$$

390 
$$\varepsilon_d = \frac{\int_0^T \max_l |S_n(l, m, t)| dt}{\int_0^T |S_{sa}(l_0, m_0, t)| dt}, \quad (15)$$



391 where  $l_0$  and  $m_0$  represent the loading harmonic degree and order,  $S_n$  and  $S_{sa}$  are solutions of load Love  
392 numbers from CitcomSVE and semi-analytical methods, respectively,  $T$  is the total model time (i.e., 40),  
393 and in equation (15) for the dispersion error,  $\max$  represents the maximum value for all the non-loading  
394 harmonic degrees  $l$  and orders  $m$ . The response should only occur at the loading harmonic for the spherically  
395 symmetric mantle structure considered here. Therefore, amplitude error  $\varepsilon_a$  measures the accuracy at the  
396 loading harmonic and dispersion error  $\varepsilon_d$  measures the accuracy at other harmonics. Note that the errors  
397 defined in equations (14) and (15) are similar to norm-1 errors.

398 Figure 2 shows the amplitude errors of load Love numbers as a function of horizontal numerical  
399 resolution (i.e., the horizontal grid size ranging from ~200 km to ~50 km at the surface for resolutions R1-  
400 R4) for all cases. For most of the calculations with different loading harmonics, the amplitude errors  
401 decrease with decreasing horizontal grid size with a slope of close to 2 in the log-log plot of Figure 2,  
402 especially for Love numbers  $h_l$  and  $k_l$ . This suggests that the error is roughly proportional to the square of  
403 the grid size, aligning with the expected second-order accuracy for trilinear elements in CitcomS (e.g.,  
404 Zhong et al., 2008). It is worth noting that from R1 to R4, the increase in vertical resolution is not  
405 proportional to the increase in horizontal resolution, which may cause the slope in Figure 2 to deviate from  
406 2. Figure 2 shows that with a horizontal resolution of ~50 km, the accuracy of CitcomSVE is better than  
407 0.1% up to spherical harmonics of degree 4 and better than 2% up to spherical harmonics of degree 16 in  
408 terms of Love numbers  $h_l$  and  $k_l$ . For Love number  $l_l$ , the errors are slightly larger than that for  $h_l$  and  $k_l$ .  
409 Compared to the benchmark results of CitcomSVE 2.1 (Zhong et al., 2022), the errors presented here are  
410 generally larger for cases with the same resolutions, which is understandable considering that CitcomSVE  
411 3.0 solves for models with higher complexity (i.e., the internal density variations caused by compressibility  
412 and density discontinuities).



413

414 Fig 2. Amplitude errors of Love numbers  $h$  (a),  $k$  (b) and  $l$  (c) as a function of numerical resolutions (i.e.,  
 415 R1-R4, corresponding to horizontal resolutions of approximately 200 to 50 km). For Love number  $k$  of  
 416 loads (1,0), all calculations with different resolutions have a relative error of less than  $10^{-5}$  and are not  
 417 shown in this figure. Note that R4 and R5 have the same horizontal but different vertical resolutions.

418

### 419 3.2. Glacial isostatic adjustment using ICE-6G and VM5a

420 This section presents the benchmark for an example GIA model with ICE-6G and VM5a (Peltier  
 421 et al., 2015). A GIA model calculation requires solving governing equations (1)-(3) together with boundary  
 422 conditions (4)-(5) and the sea-level equation (11) to determine time-dependent gravitational anomalies and  
 423 displacements at the Earth's surface and sea level changes. As discussed in section 2.3, to deal with the  
 424 non-linear nature of the sea level equation, multiple iterations of complete GIA model runs may be needed  
 425 (Kendall et al., 2005). Before presenting benchmark results for CitcomSVE 3.0 against the semi-analytical  
 426 method, we will first demonstrate how the one-iteration solution method discussed in section 2.3 may be  
 427 used to achieve adequate accuracy of GIA solutions using the semi-analytical method.

#### 428 3.2.1. A one-iteration solution method for the sea level equation.

429 We have implemented the multiple outer iteration algorithm by Kendall et al., (2005) for the sea  
 430 level equation in our semi-analytical code (A et al., 2013). For ICE-6G and VM5a, calculation K3 represents  
 431 the reference case with convergent solutions after three outer iterations, based on Kendall's original  
 432 approach. The normalized ocean area which is a measure of the ocean function  $O(t)$  for K3 varies between  
 433  $\sim 0.66$  at the last glacial maximum (LGM) and  $\sim 0.71$  at 122 kybp and the present-day (Fig. S1). Figure S1  
 434 also shows the ocean area after the first outer iteration for calculation K3, which, denoted as K1, differs



435 significantly from that of K3. Calculation AS1 represents a single outer iteration model run using our pre-  
436 calculated ocean function  $O(t)$  as discussed in section 2.3, and AS2 represents the results from the second  
437 outer iteration after AS1 using the updated ocean functions  $O(t)$  and initial topography  $T_0$ , Figure S1 clearly  
438 demonstrates that AS1, different from K1, is very similar to K3 and AS2, while the latter two are identical,  
439 indicating that the ocean function  $O(t)$  for our first outer iteration (AS1) is a fairly accurate representation  
440 of the convergent solutions of the Kendall's original approach (K3). Note that the present-day topography  
441 is used as initial topography  $T_0$  for calculations AS1 and K1.

442 Using RSL from K3 as standard results, Fig. S2 shows that the maps of RSL difference (i.e., the  
443 accuracy) to K3 from calculations AS1, K1 and AS2 at 5 kybp, 10 kybp and 15 kybp. The absolute error in  
444 RSL from AS1 is negligibly small for most regions (Fig. S2a, S2d and S2g), whereas the absolute error  
445 from K1 is much worse, especially at 20 kybp (Fig. S2h). AS2 is identical to K3, the standard results (Fig.  
446 S2c, S2f and S2i). Admittedly, there are relatively large errors in some localized regions for AS1, such as  
447 Hudson Bay and the Arctic Ocean near Fennoscandia for some periods (Fig. S2a and S2d), because we  
448 ignore the change in surface radial displacement when deriving the pre-calculated ocean function used in  
449 AS1. However, the largest errors in those areas mostly occur in the ocean, while along the coastlines where  
450 paleo-relative sea level records are available, the absolute errors are all less than 10 meters (Fig. S2a and  
451 S2d). Figure S3 shows the modeled RSL curves at four representative sites including Hudson Bay and  
452 Fennoscandia from K3, K1, AS1 and AS2 calculations. The results are consistent with that from Figure S2  
453 in that the errors in modeled RSL from AS1 (i.e., the single outer iteration model run using our revised  
454 method for ocean functions) are negligible, whereas the errors from K1 are evident, especially for far-field  
455 sites. Note that even at Churchill, which is on the coastline of Hudson Bay, AS1 has negligible errors in  
456 RSL calculations.

457 To further assess the errors in RSL from our AS1 model, we tested two additional GIA calculations  
458 with extremely strong or weak mantle viscosity models. For both cases, the lithospheric thickness is 100  
459 km. For the strong mantle case, the entire mantle below the lithosphere has a viscosity of  $5 \times 10^{22}$  Pas. For



460 the weak mantle case, the 200 km thick asthenosphere below the lithosphere and the rest of the mantle have  
461 viscosities of  $5 \times 10^{18}$  Pas and  $10^{20}$  Pas, respectively. Figure S4 shows similarly small errors for both cases  
462 to that of VM5a (Fig. S2), indicating the reliability of our AS1 model.

463 Other pre-calculated ocean functions  $O(t)$  for any given ice model may be constructed to obtain  
464 more accurate RSL results in our AS1 method by replacing the “rigid Earth” approximation with others,  
465 for example, the isostasy approximation in which surface elevation changes to compensate the surface  
466 loads. Another possible way is to perform a full GIA modeling with three outer iterations (i.e., for outer  
467 iterations to converge) for a reference viscosity model and use the ocean functions from the last outer  
468 iteration as the pre-calculated ocean functions for any other GIA calculations with reasonable viscosity  
469 models in our AS1 method. We test such a strategy by using a reference viscosity model which has a 100-  
470 km thick elastic lithosphere and its underlying mantle with a uniform viscosity of  $10^{21}$  Pas and then applying  
471 the resulting pre-calculated ocean functions for those same two GIA cases with extremely strong or weak  
472 viscosity models as in Figure S4. The resulting errors in RSL for those two cases (Fig. S5) are similar to  
473 that in Figure S4 for which the “rigid Earth” approximation was used in building the pre-calculated ocean  
474 functions.

475 To quantify the upper bound of errors in RSL by using one outer iteration (e.g., our AS1 method),  
476 we compute 806 GIA models covering a wide range of mantle viscosities and determine RSL histories for  
477 a large number of sites in three regions including North America, Fennoscandia, and far fields using both  
478 AS1 and K3 methods. The numbers of sites are 18, 12, and 36 for North America, Fennoscandia, and far  
479 fields, respectively. The North American and Fennoscandian sites are from Peltier et al., (2015), and the  
480 far-field sites are from Lambeck et al., (2014). These models, same as those in Kang et al., (2024), have  
481 three viscosity layers: a lithosphere of 100 km thick, the upper and lower mantles, and use ICE-6G\_D as  
482 the ice history (Peltier et al., 2015, 2018). The viscosity varies from  $10^{19}$  Pas to  $10^{21.5}$  Pas in the upper  
483 mantle and from  $10^{20.5}$  Pas to  $10^{23.5}$  Pas in the lower mantle. The relative error (i.e., the relative difference



484 from the reference case K3) in modeled RSL for each site is defined as  $\epsilon_i = \frac{\int_0^T |RSL_{x,i}(t) - RSL_{K3,i}(t)| dt}{\int_0^T |RSL_{K3,i}(t)| dt}$ , where  
485  $RSL_{x,i}$  is the modeled RSL at site  $i$  for case K1, AS1, or AS2,  $RSL_{K3,i}$  is for the reference case K3, and the  
486 integral is for the total model time duration. The regionally averaged relative error  $\epsilon$  is defined as the  
487 average error among all sites within each region, i.e.,  $\epsilon = \Sigma \epsilon_i / N$ , where  $N$  is the total number of sites within  
488 each region. The maximum regionally averaged relative error among those 806 GIA models is less than 5%  
489 (Supplement Table 2) for our AS1 method.

490 We also quantify the maximum absolute error in RSL, defined as the maximum of  $|RSL_x(t) -$   
491  $RSL_{K3}(t)|$  among all time periods  $t$  and all sites in each region from those 806 calculations (Supplement  
492 Table 2). For far-field sites where RSL is mainly controlled by ocean functions and ice volume changes,  
493 the maximum absolute error in RSL is less than 3 meters for the AS1 method but more than 10 meters for  
494 the K1 method, consistent with Fig. S1 in that AS1 provides more accurate ocean functions than K1.  
495 However, the maximum absolute error in near-field RSL is more significant and up to ~23 meters for both  
496 AS1 and K1 methods, reflecting the fact that near-field ocean functions and paleo-topography are more  
497 affected by visco-elastic deformation. Fig. S6 shows the RSL curves for the site and viscosity model  
498 corresponding to the maximum absolute error of ~23 meters in RSL for AS1. Note that at the site for this  
499 case with the maximum absolute error, the total RSL change exceeds 600 meters and the RSL from AS1 is  
500 not significantly different from that from K3 (Fig. S6). Depending on factors including the user's goal, RSL  
501 data quality, and requirements for accuracy and efficiency of GIA calculations, AS1 could be a viable  
502 method to obtain reliable RSL in both far fields and near fields with minimal computational cost.

503 We summarize our attempts to get accurate RSL results from a single complete GIA model run as  
504 follows. Since the purpose of multiple outer iterations is to update ocean function history and initial  
505 topography successively to be consistent with the present-day topography and a given ice model (Kendall  
506 et al., 2005), our strategy is to construct pre-calculated ocean functions and initial topography that would  
507 lead to RSL solutions with an adequate level of accuracy with a single complete GIA model run (i.e., the



508 AS1 method). The present-day topography would be a good approximation for initial topography if a model  
509 starts with an ice-sheet distribution similar to that of the present day (i.e., the interglacial period), as in the  
510 benchmark study here. We found that three outer iterations of complete model runs with successively  
511 updated ocean functions and initial topography could be replaced with our AS1 method, depending on  
512 users' goals and requirements for the error levels. For example, studies on global properties of RSL could  
513 achieve adequately accurate results from one single complete run (i.e., AS1) with properly constructed pre-  
514 calculated ocean functions, as we discussed. If the goal is to model the RSL for one particular near-field  
515 site as accurately as possible, it would be more prudent to run two or three outer iterations of complete GIA  
516 runs with successively updated ocean functions and initial topography following Kendall et al. (2005). It is  
517 worthwhile to mention that, when modeling RSL changes, one should also consider other factors including  
518 the errors in RSL records (often exceeding 10 m in near field during the rapid deglaciation (Peltier et al.,  
519 2015; Lambeck et al., 2017)), the relatively low resolution of global ice models, inherent numerical errors,  
520 and unaccounted processes in the current sea level equation (e.g., erosion and sedimentation).

521 Our above-mentioned results are particularly relevant for numerical modeling given its  
522 computational cost. CitcomSVE 3.0 fully supports the multiple outer iteration approach using pre- and post-  
523 processes to update ocean functions and initial topography. In the following GIA benchmark, we compare  
524 the results from a single complete CitcomSVE model run with our semi-analytic solutions of the first outer  
525 iteration (i.e., AS1), using the pre-calculated ocean functions constructed by assuming the "rigid Earth" and  
526 the present-day topography as the initial topography. This comparison ensures that CitcomSVE and semi-  
527 analytic calculations have the same ocean functions and initial topography, such that the differences in  
528 solutions between CitcomSVE and semi-analytical methods are solely related to numerical errors rather  
529 than differences in the models.

### 530 3.2.2. Definition of the GIA problem.

531 Since one of the most important applications for CitcomSVE is to model the GIA processes, it is  
532 essential to perform a benchmark with glaciation-deglaciation history as surface loads, considering the





533 effects of polar wander, apparent center of mass motion and ocean loads determined by the sea-level  
534 equation. Note that the same type of benchmark has been published for the incompressible version  
535 CitcomSVE 2.1 (Zhong et al., 2022), and we largely follow the setups of that previous work except that the  
536 current calculations consider mantle compressibility (i.e., the PREM model), and that the updated sea level  
537 equation is used as discussed in the last sub-section (i.e., the AS1 method). The Earth model used in this  
538 case is the same as the one used for single harmonic loading examples in the previous section.

539 In this case, the surface load consists of a full glaciation-deglaciation cycle, based on the ICE-6G\_D  
540 ice model (Peltier et al., 2015, 2018) that includes the last 122 thousand years from the last interglacial  
541 period to the present day. We assume that Earth was in an equilibrium state at the onset of loading (i.e., 122  
542 kybp), and that the surface displacements and gravitational potential anomalies since 122 kybp are induced  
543 by ice height variations relative to the initial stage and the corresponding change in ocean loads. We  
544 computed six cases using CitcomSVE 3.0 with different spatial-temporal resolutions and cut-off values for  
545 the maximum spherical harmonic degrees used in calculating gravitational potential (Table 3). Cases  
546 GIA\_R1, GIA\_R2, and GIA\_R3 have spatial resolutions of 135 km, 81 km, and 50 km (i.e., a total number  
547 of elements of 12x48x48x48, 12x48x80x80, and 12x64x128x128), respectively, and a temporal resolution  
548 of 125 years per step. Case GIA\_R3\_LT is the same as GIA\_R3 except with a longer time increment of  
549 250 years per step before LGM (i.e., 26 kybp). Cases GIA\_R3\_LT\_SH20 and GIA\_R3\_LT\_SH64 have a  
550 cut-off value of 20 and 64 for the maximum spherical harmonic degrees, respectively, compared to 32 for  
551 other cases. Note that same as CitcomSVE 2.1 (Zhong et al., 2022), computing gravitational potential in  
552 the spherical harmonic domain can be computationally expensive. On the other hand, the semi-analytical  
553 solution is obtained using spherical harmonic degrees and orders up to 256.

554 It should be noted that in the current implementation, CitcomSVE reads in ice loads defined on  
555 regular grids (e.g., 1°x1° grid) and then interpolates the loads to the irregular finite element grids, whereas  
556 semi-analytical calculations use spherical harmonic expansions of ice loads to a maximum spherical  
557 harmonic degree and order (i.e., 256 in this study) as inputs. The interpolation may cause inconsistent



558 representations of ice loads between CitcomSVE and the semi-analytical calculations. To understand the  
 559 potential error resulting from the interpolation, we test another case GIA\_R3B, which is the same as  
 560 GIA\_R3 except that, for this case, we let CitcomSVE read in ice loads that are computed on CitcomSVE  
 561 finite element grid points from summing up all the spherical harmonics as used for the analytical solutions,  
 562 thus avoiding the interpolation from the regular grids to the finite element grids and assuring that  
 563 CitcomSVE calculations use the exactly same ice loads as that for analytical solutions.

564

565 **Table 3: Relative Errors for Surface 3-Component Displacement Rates for GIA Benchmark**

	GIA_R1	GIA_R2	GIA_R3	GIA_R3B <sup>a</sup>	GIA_R3_LT <sup>b</sup>	GIA_R3_LT_SH20 <sup>c</sup>	GIA_R3_LT_SH64
Resolution	48x48x48	48x80x80	64x128x128	64x128x128	64x128x128	64x128x128	64x128x128
Total steps	976	976	976	976	592	592	592
# Cores	96	96	384	384	192	192	384
CPU hours	5.57 <sup>d</sup>	4.89	3.01	3.13	3.88	3.34	3.77
$\epsilon_r(0)^e$	17.1% (15.8%) <sup>f</sup>	8.7% (8.1%)	4.7% (4.4%)	4.4% (3.8%)	4.6% (4.4%)	5.0% (4.8%)	4.7% (4.4%)
$\epsilon_h(0)$	14.8% (15.0%)	6.9% (6.9%)	3.9% (3.9%)	3.5% (3.4%)	3.9% (3.9%)	3.9% (3.9%)	3.9% (3.9%)
$\epsilon_r(15)$	7.9% (6.7%)	4.5% (4.1%)	3.1% (3.0%)	2.8% (2.3%)	3.1% (3.0%)	3.1% (3.0%)	3.2% (3.0%)
$\epsilon_h(15)$	4.4% (3.9%)	2.6% (2.4%)	1.7% (1.7%)	1.6% (1.5%)	1.7% (1.7%)	1.7% (1.7%)	1.7% (1.7%)
$\epsilon_r(26)$	7.9% (6.6%)	3.8% (3.3%)	2.5% (2.3%)	2.3% (1.8%)	3.1% (3.0%)	3.0% (2.9%)	3.2% (3.1%)
$\epsilon_h(26)$	4.4% (3.9%)	2.3% (2.0%)	1.3% (1.3%)	1.4% (1.1%)	1.9% (1.8%)	1.9% (1.8%)	1.9% (1.9%)

566

567 <sup>a</sup> The differences between cases GIA\_R3B and GIA\_R3 are discussed in section 3.2.2.

568 <sup>b</sup> The “LT” in GIA\_R3\_LT represents larger time increments between time steps, where the increments are  
 569 250 years and 125 years before and after 26 kybp, respectively. Cases GIA\_R1, GIA\_R2, and GIA\_R3  
 570 have uniform time increment of 125 years.

571 <sup>c</sup> The “SH20” in GIA\_R3\_LT\_SH20 represents that the cut-off of degrees and orders of spherical harmonics  
 572 in this calculation is 20. Similarly, case GIA\_R3\_LT\_SH64 has cut off at degrees and orders of 64. Other  
 573 cases are cut off at degrees and orders of 32.

574 <sup>d</sup> For this case, the solution converges slowly, causing larger CPU time. All the cases are computed on the  
 575 NCAR supercomputer Derecho.

576 <sup>e</sup>  $\epsilon_r$  and  $\epsilon_h$  are errors of displacement rates in radial and horizontal directions, respectively. The errors are  
 577 given at present-day (0), 15 kybp, and 26 kybp (indicated by numbers inside parentheses).

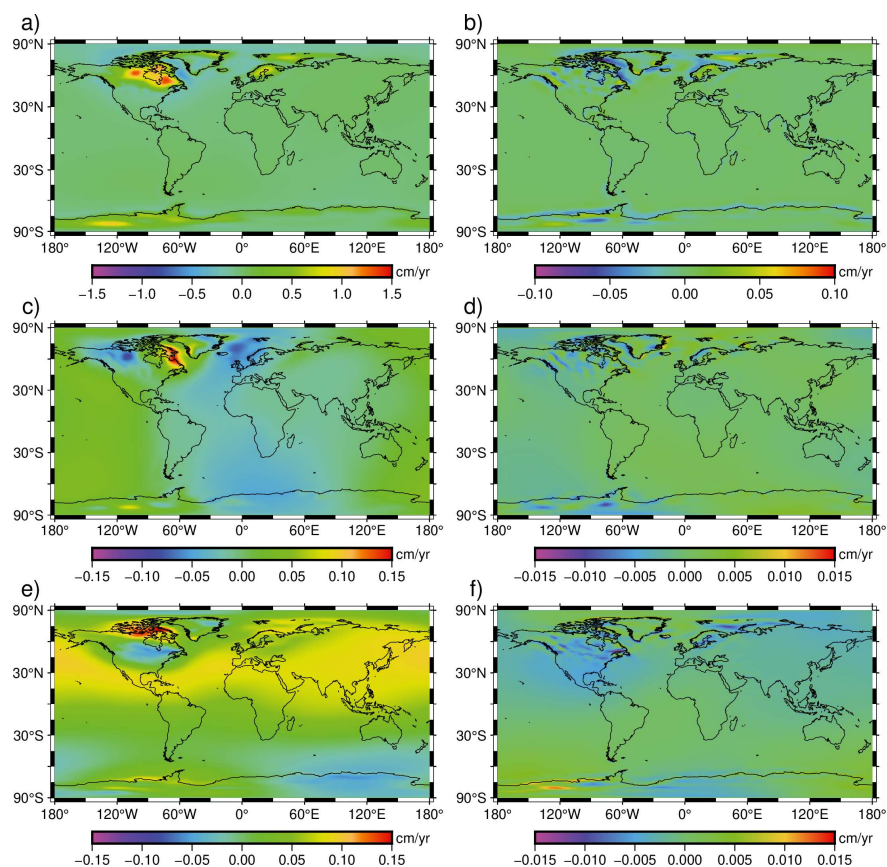
578 <sup>f</sup> Numbers out of parentheses are errors calculated based on regular grids, whereas numbers inside of  
 579 parentheses are calculated based on CitcomSVE grids.

580



581 3.2.3. Benchmark results.

582 We compare the 3-component displacement rates at the surface for three different times (i.e., the  
583 present-day, 15 kybp, and 26 kybp) obtained from CitcomSVE and the semi-analytical code. Figure 3 shows  
584 the present-day displacement rate in vertical, eastern, and northern directions for case GIA\_R3 from  
585 CitcomSVE. Large uplift rates at the present day occur in North America, Fennoscandia, and West  
586 Antarctica (Fig. 3a), suggesting ongoing rebound induced by ice melting since the last glacial maximum in  
587 these regions. Horizontal displacement rates usually have much smaller amplitudes than that in radial  
588 direction in those regions.



589

590



591 Figure 3. Displacement rates at the present day from case GIA\_R3 in radial (a), eastern (c), and northern  
592 (e) directions and the differences to analytical solutions for radial (b), eastern (d), and northern (f)  
593 directions.

594

595 Figure 3 also shows the differences in present-day displacement rates between CitcomSVE and  
596 semi-analytical solutions. The differences are small compared with the magnitudes of displacement rates.  
597 Relatively large magnitudes of errors are mainly on short wavelengths (e.g. localized regions), which may  
598 partially reflect the fact that CitcomSVE tends to have poorer accuracy at shorter wavelengths (Fig. 1 and  
599 2). Following Zhong et al. (2022), we define relative RMS differences (i.e., errors) in displacement rates  
600 between CitcomSVE and semi-analytical solutions as:

$$601 \quad \varepsilon(t) = \sqrt{\frac{\sum [f_{FE}(\theta, \varphi, t) - f_S(\theta, \varphi, t)]^2}{\sum [f_S(\theta, \varphi, t)]^2}}, \quad (16)$$

602 where  $f_{FE}(\theta, \varphi, t)$  and  $f_S(\theta, \varphi, t)$  are the fields of interest at a given time  $t$  from CitcomSVE and semi-  
603 analytical solutions, respectively, and the summation is based on a regular  $1^\circ$ -by- $1^\circ$  grid. To interpolate the  
604 CitcomSVE solutions onto the regular grid, we use the near neighbor method provided by GMT (Wessel et  
605 al., 2019). We also report errors calculated by unweighted summation on the CitcomSVE grid, given the  
606 relatively uniform grid size on the spherical surface in CitcomSVE, and the differences in errors from these  
607 two ways of calculation are insignificant. We compute errors for radial and horizontal components at three  
608 times: the present-day, 15 kybp and 26 kybp. Note that for horizontal error, we square the difference for  
609 each horizontal component (i.e., north and east) and add them together for each location.

610 Table 3 lists the errors for displacement rates at these three times for all cases, together with the  
611 total CPU time and number of CPUs used for each case. The errors decrease significantly from GIA\_R1 to  
612 GIA\_R3. For Cases GIA\_R3, the errors of displacement rates are less than 5%. Case GIA\_R3B, which  
613 avoids the interpolation of the input ice loads from the regular input grid into CitcomSVE finite element  
614 grid to eliminate the potential inconsistency in ice loads between CitcomSVE and semi-analytical  
615 calculations, has slightly smaller errors than GIA\_R3, indicating a relatively small error induced by the



616 interpolation. Case GIA\_R3\_LT with larger time resolution before 26 kybp has larger errors in  
617 displacement rates at 26 kybp but similar error levels at 15 kybp and present day. Those errors are close to  
618 those from CitcomSVE 2.1 (Zhong et al., 2022). CitcomSVE 3.0 is about three times slower than  
619 CitcomSVE 2.1 for the same resolutions since internal density variations make the computation more  
620 expensive, as discussed in section 2.2. We found that for cases GIA\_R1, GIA\_R2, and GIA\_R3, calculating  
621 gravitational potential anomalies takes about one-fourth to half of the total calculation times, depending on  
622 the time spent solving the displacement field. It is possible to speed up the calculations of the gravitational  
623 potential anomalies by using a grid-based method (e.g., Latychev et al., 2005) or direct integration (e.g.,  
624 Wang and Li, 2021) for the Poisson equation instead of the currently used spherical harmonic transform.  
625 However, the maximum degree of spherical harmonics, varying from 20 to 64, has insignificant effects on  
626 surface displacement (Tables 3 and 4), although it would affect the modeled change rates of geoid and  
627 gravity.

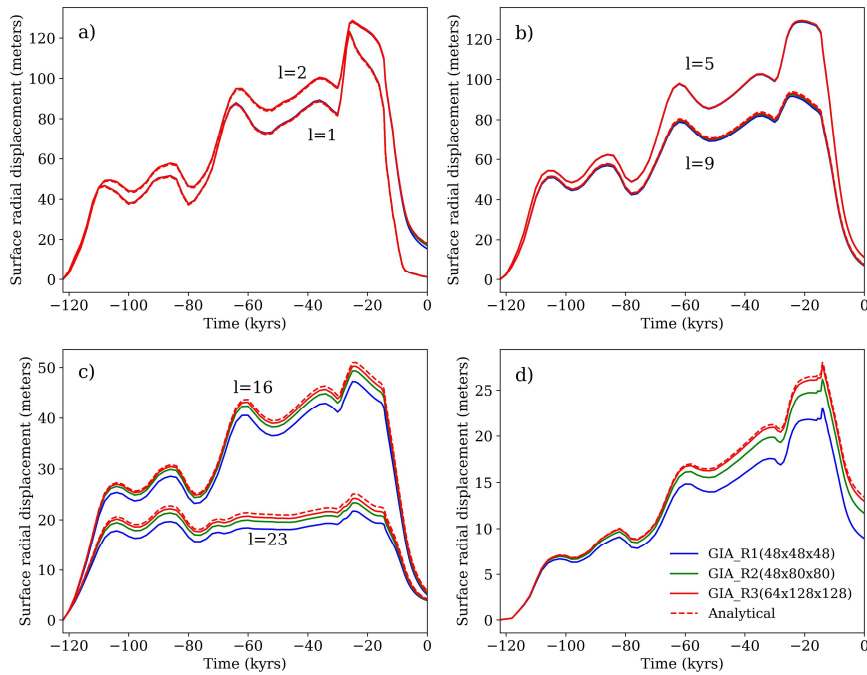
628 We also compare the cumulative radial displacements at different spherical harmonic degrees from  
629 CitcomSVE and semi-analytical solutions, following previous works (Paulson et al., 2005; A et al., 2013;  
630 Kang et al., 2022; Zhong et al., 2022). The spherical harmonic coefficients of the surface displacement field  
631 are provided as an output of CitcomSVE (see Zhong et al., 2022, for the spherical harmonic expansion used  
632 in CitcomSVE). The degree amplitude for each  $l$  is calculated by

$$633 \quad a_l(t) = \sqrt{\frac{1}{l+1} \sum_{m=0}^l [C_{lm}(t)^2 + S_{lm}(t)^2]} \quad , \quad (17)$$

634 where  $C_{lm}$  and  $S_{lm}$  denote the cosine and sine parts of the spherical harmonic coefficients expanded from  
635 the radial displacement fields at time  $t$ . Figures 4a-4c show the amplitude  $a_l$  of surface radial displacement  
636 at selected spherical harmonics degrees ( $l=1, 2, 5, 9, 16$  and  $23$ ) for the three CitcomSVE cases, together  
637 with the corresponding semi-analytical solutions. Same as CitcomSVE 2.1 (Zhong et al., 2022), the lowest-  
638 resolution case is adequate for relatively long wavelengths ( $l=1, 2, 5,$  and  $9$ ), whereas higher resolution  
639 models are required for accuracy in shorter wavelengths ( $l=16$  and  $23$ ) (Fig. 4c). Figure 4d shows the results



640 for the harmonic of  $l=2$  and  $m=1$  that corresponds to the polar wander. Similar to findings from single  
 641 harmonic benchmarks in the previous section and Zhong et al., (2022), high spatial resolution is required  
 642 to obtain an accurate solution for the polar wander term. Note that the amplitudes of polar wander mode  
 643 are much smaller than other long wavelength modes like  $l=2$ , 5, and 9.



644  
 645 Figure 4. Amplitudes of cumulative radial surface displacement at different spherical harmonic degrees as  
 646 a function of time for the semi-analytical solutions (Analytical) and three CitcomSVE calculations  
 647 (GIA\_R1, GIA\_R2, and GIA\_R3) for  $l=1,2$  (a),  $l=5,9$  (b),  $l=16, 23$  (c), and polar wander mode with  $l=2$ ,  
 648  $m=1$  (d).

649

650 Following Zhong et al., (2022), we use the time-integrated relative error of degree amplitude  $\epsilon_l$  to  
 651 quantify the time-averaged error for a given degree  $l$ .  $\epsilon_l$  is defined as

652

$$\epsilon_l = \sqrt{\frac{\int_0^T [a_{lFE}(t) - a_{lS}(t)]^2 dt}{\int_0^T a_{lS}(t)^2 dt}}, \quad (18)$$



653 where  $a_{l_{FE}}(t)$  and  $a_{l_s}(t)$  represent the degree amplitudes at time  $t$  from the CitcomSVE and semi-  
654 analytical solutions, respectively, and  $T$  is the entire calculation period. The errors for each case are shown  
655 in Table 4. As expected, the errors decrease with increasing spatial resolution for each degree, and errors  
656 for shorter wavelengths are larger than those for longer wavelengths, except for the polar wander term with  
657 relatively large errors.

658 **Table 4 Relative Errors for Surface Radial Displacements at Different Harmonics**

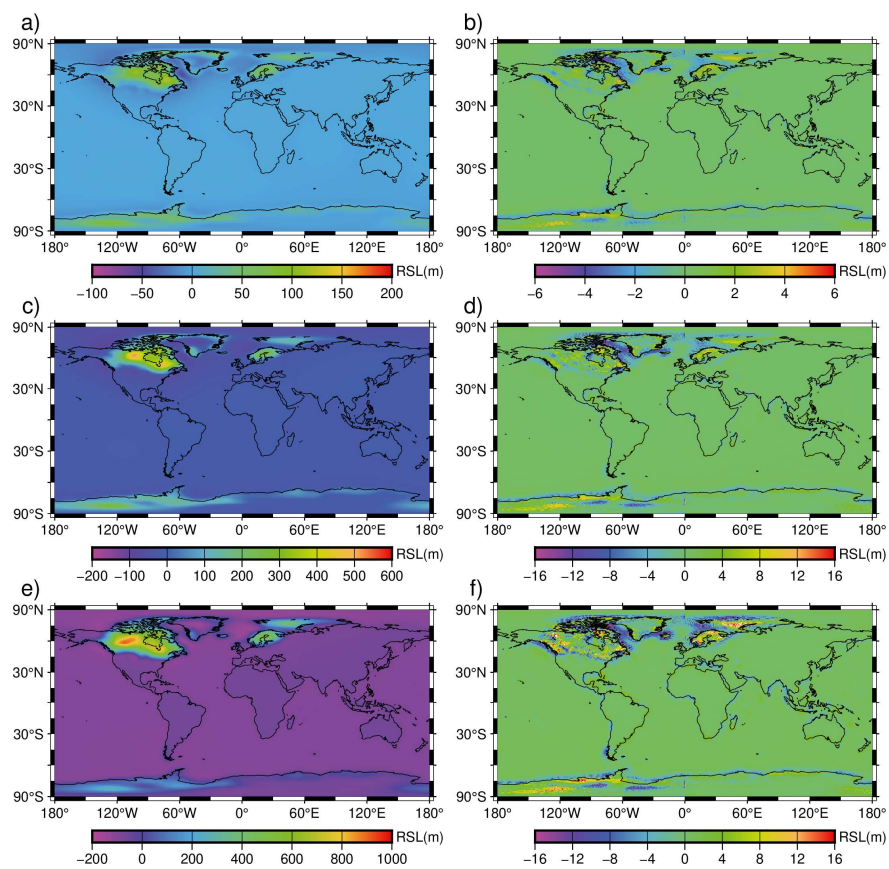
	GIA_R1	GIA_R2	GIA_R3	GIA_R3_LT	GIA_R3_LT_SH20	GIA_R3_LT_SH64
$\epsilon_1$	0.97%	0.74%	0.62%	0.64%	0.64%	0.64%
$\epsilon_2$	0.98%	0.76%	0.73%	0.74%	0.74%	0.72%
$\epsilon_5$	0.33%	0.12%	0.13%	0.14%	0.14%	0.14%
$\epsilon_9$	2.30%	1.37%	0.77%	0.77%	0.77%	0.77%
$\epsilon_{16}$	7.56%	3.30%	1.45%	1.45%	1.45%	1.45%
$\epsilon_{23}$	13.66%	6.69%	3.10%	3.10%	N/A <sup>b</sup>	3.10%
$\epsilon_{2,1}$ <sup>a</sup>	17.53%	6.58%	1.48%	1.39%	1.39%	1.80%

659 <sup>a</sup>  $\epsilon_{2,1}$  represents the errors for the polar wander term ( $l=2, m=1$ ).

660 <sup>b</sup> N/A, the cut-off of degrees and orders of spherical harmonics is 20 for this case and we only output the  
661 spherical harmonics up to the cut-off value in CitcomSVE.

662

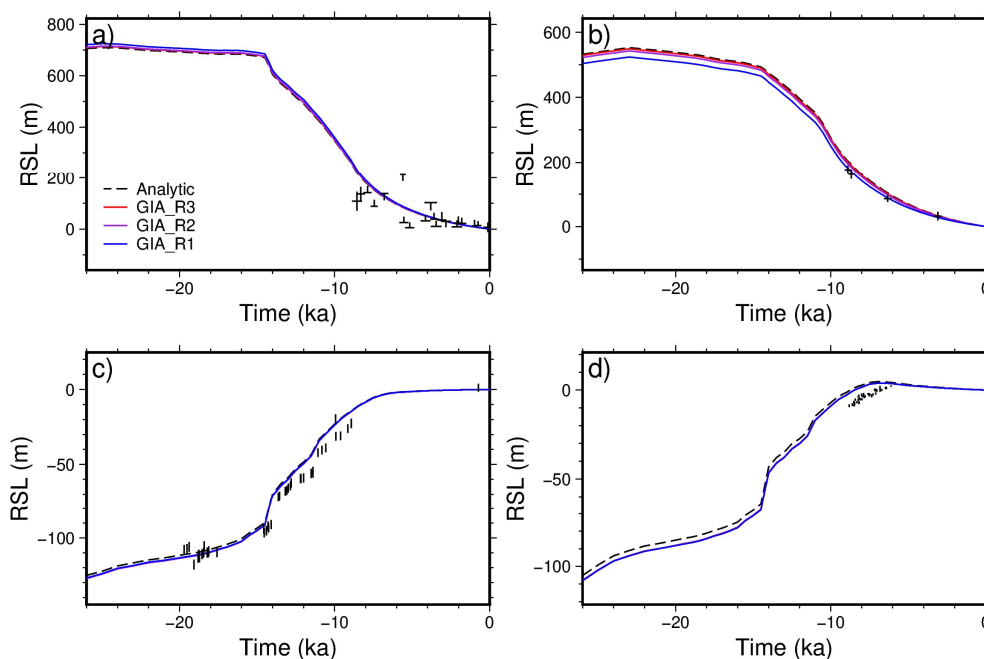
663 Figure 5 shows the comparisons of modeled relative sea levels at different periods (5 kybp, 10  
664 kybp, and 15 kybp) for GIA\_R3 and the semi-analytical solutions on map views. The globally averaged  
665 relative misfits at 5 kybp, 10 kybp, and 15 kybp are 4.14%, 2.82%, and 1.70%, respectively, similar to  
666 errors in displacement rates. The regions with localized, relatively large errors (Fig. 5b, 5d, and 5f) are  
667 mostly around the edges of ice sheets in North America, Fennoscandia, and Antarctica, similar to that for  
668 displacement rates, as shown in Figure 3b. Figure 6 compares modeled RSL curves for several sites from  
669 semi-analytical solutions and three CitcomSVE calculations with different spatial resolutions. Increasing  
670 spatial resolution reduces the misfits to semi-analytical solutions for near-field sites (i.e., sites close to ice  
671 sheets) (Fig. 6a and 6b), but does not appear to affect the far-field solutions as much (Fig. 6c and 6d).



672

673 Figure 5. Map of modeled relative sea level at 5 kybp (a), 10 kybp (c), and 15 kybp (e) from GIA\_R3 and  
674 their differences to semi-analytic solutions at 5 kybp (b), 10 kybp (d), and 15 kybp (f), respectively.





675

676 Figure 6. Relative sea-level curves for the last 26 ky at four sites from semi-analytic solutions (Analytic)  
677 and three CitcomSVE calculations of different resolutions: cases GIA\_R1, GIA\_R2, and GIA\_R3. The four  
678 sites are Churchill (a), Vasterbotten (b), Barbados (c), and Geylang (d) with longitudes and latitudes of  
679 (265.60, 58.70), (19.90, 64.00), (300.45, 13.04), and (103.87, 1.31), respectively. The symbols represent the  
680 observed RSL changes. The observed RLS are from Peltier et al., (2015) and Lambeck et al., (2014).

681

#### 682 4. Conclusion and Discussion

683 This study introduces CitcomSVE-3.0, an enhanced finite element package that builds upon its  
684 predecessor, CitcomSVE-2.1 (Zhong et al., 2022), an efficient package that utilizes massively parallelized  
685 computers with up to thousands of CPUs. The new version incorporates elastic compressibility (e.g., the  
686 PREM) based on the work of A et al. (2013) and improves the algorithm for solving sea level equations  
687 following the work of Kendall et al. (2005), which considers the changes in ocean loads and ocean functions  
688 related to ocean-continent transitions and the existence of floating ice. Two benchmark problems are



689 computed with different numerical resolutions: 1) surface loads of different single harmonics and 2) GIA  
690 problem with ICE6G ice model.

691 Extensive comparisons between CitcomSVE-3.0 calculations and semi-analytic solutions are  
692 presented to validate the accuracy of the CitcomSVE package. The accuracy of CitcomSVE with a  
693 horizontal resolution of  $\sim 50$  km is better than 0.1% up to spherical harmonics of degree 4 and better than  
694 2% up to degree 16 in vertical motion and gravitational potential for single harmonic loading problems. We  
695 show that CitcomSVE has a second order of accuracy, i.e., the errors would be reduced to 1/4 if element  
696 sizes were reduced by a factor of two. For GIA problems with realistic ice models and dynamically  
697 determined ocean loads, the average errors for CitcomSVE models with  $\sim 50$  km horizontal resolution are  
698 less than 5% in displacement rates and relative sea levels.

699 As shown in the benchmark work for CitcomSVE-2.1 (Zhong et al., 2022), CitcomSVE has a  
700 parallel computation efficiency of  $> 75\%$  for up to 6144 CPU cores. With its accuracy and efficiency in  
701 modeling viscoelastic response to surface loads and tidal forces, the open-source package CitcomSVE has  
702 the ability to advance research in planetary and climatic sciences, including GIA-related problems.

703

704

705

706 **Acknowledgement:** This work is supported by NSF through grant numbers NSF-EAR 2222115 and NSF-  
707 OPP 2333940. Our calculations were performed on parallel supercomputer Derecho operated by the  
708 National Center for Atmospheric Research under CISL project codes UCUD0007.

709

710 **Code and Data Availability Statement:** The updated CitcomSVE package can be downloaded from  
711 <https://github.com/shjzhong/CitcomSVE>. The input files and results to produce figures and tables for this



712 study can be downloaded from <https://doi.org/10.5281/zenodo.13932411> (Yuan, 2024). The original ICE-

713 6G ice history model is from <https://www.atmosph.physics.utoronto.ca/~peltier/data.php>.

714

715 **Author contribution:** All authors contributed to the development of the code, design of the research,  
716 analysis of the results, and writing of the manuscript. T.Y. performed numerical calculations.

717

718 **Competing interests:** The authors declare there are no competing interests in this work.



## 719 Reference

- 720 A, G., Wahr, J., and Zhong, S.: Computations of the viscoelastic response of a 3-D compressible Earth to  
721 surface loading: an application to Glacial Isostatic Adjustment in Antarctica and Canada, *Geophysical*  
722 *Journal International*, 192, 557–572, <https://doi.org/10.1093/gji/ggs030>, 2013.
- 723 Bagge, M., Klemann, V., Steinberger, B., Latinović, M., and Thomas, M.: Glacial-Isostatic Adjustment  
724 Models Using Geodynamically Constrained 3D Earth Structures, *Geochemistry, Geophysics, Geosystems*,  
725 22, e2021GC009853, <https://doi.org/10.1029/2021GC009853>, 2021.
- 726 Bevis, M., Wahr, J., Khan, S. A., Madsen, F. B., Brown, A., Willis, M., Kendrick, E., Knudsen, P., Box, J.  
727 E., van Dam, T., Caccamise, D. J., Johns, B., Nylén, T., Abbott, R., White, S., Miner, J., Forsberg, R., Zhou,  
728 H., Wang, J., Wilson, T., Bromwich, D., and Francis, O.: Bedrock displacements in Greenland manifest ice  
729 mass variations, climate cycles and climate change, *Proceedings of the National Academy of Sciences*, 109,  
730 11944–11948, <https://doi.org/10.1073/pnas.1204664109>, 2012.
- 731 Farrell, W. E. and Clark, J. A.: On Postglacial Sea Level, *Geophysical Journal International*, 46, 647–667,  
732 <https://doi.org/10.1111/j.1365-246X.1976.tb01252.x>, 1976.
- 733 Fienga, A., Zhong, S., Mémin, A., and Briaud, A.: Tidal dissipation with 3-D finite element deformation  
734 code CitcomSVE v2.1: comparisons with the semi-analytical approach, in the context of the Lunar tidal  
735 deformations, *Celest Mech Dyn Astron*, 136, 43, <https://doi.org/10.1007/s10569-024-10202-6>, 2024.
- 736 French, S. W. and Romanowicz, B.: Broad plumes rooted at the base of the Earth’s mantle beneath major  
737 hotspots, *Nature*, 525, 95–99, <https://doi.org/10.1038/nature14876>, 2015.
- 738 Gomez, N., Latychev, K., and Pollard, D.: A Coupled Ice Sheet–Sea Level Model Incorporating 3D Earth  
739 Structure: Variations in Antarctica during the Last Deglacial Retreat, *Journal of Climate*, 31, 4041–4054,  
740 <https://doi.org/10.1175/JCLI-D-17-0352.1>, 2018.
- 741 Han, D. and Wahr, J.: The viscoelastic relaxation of a realistically stratified earth, and a further analysis of  
742 postglacial rebound, *Geophysical Journal International*, 120, 287–311, <https://doi.org/10.1111/j.1365-246X.1995.tb01819.x>, 1995.
- 744 Huang, P., Steffen, R., Steffen, H., Klemann, V., Wu, P., van der Wal, W., Martinec, Z., and Tanaka, Y.:  
745 A commercial finite element approach to modelling Glacial Isostatic Adjustment on spherical self-  
746 gravitating compressible earth models, *Geophysical Journal International*, 235, 2231–2256,  
747 <https://doi.org/10.1093/gji/ggad354>, 2023.
- 748 Ivins, E. R., van der Wal, W., Wiens, D. A., Lloyd, A. J., and Caron, L.: Antarctic upper mantle rheology,  
749 *Geological Society, London, Memoirs*, 56, 267–294, <https://doi.org/10.1144/M56-2020-19>, 2023.
- 750 Kang, K., Zhong, S., Geruo, A., and Mao, W.: The effects of non-Newtonian rheology in the upper mantle  
751 on relative sea level change and geodetic observables induced by glacial isostatic adjustment process,  
752 *GEOPHYSICAL JOURNAL INTERNATIONAL*, 228, 1887–1906, <https://doi.org/10.1093/gji/ggab428>,  
753 2022.
- 754 Kang, K., Yuan, T., and Zhong, S.: Constraints of Relative Sea Level Change on the Mantle Viscosity and  
755 the Late Pleistocene Deglaciation History, *Journal Geophysical Res.-Solid Earth*, in review, 2024.



- 756 Kendall, R. A., Mitrovica, J. X., and Milne, G. A.: On post-glacial sea level - II. Numerical formulation  
757 and comparative results on spherically symmetric models, *Geophysical Journal International*, 161, 679–  
758 706, <https://doi.org/10.1111/j.1365-246X.2005.02553.x>, 2005.
- 759 Klemann, V., Martinec, Z., and Ivins, E. R.: Glacial isostasy and plate motion, *Journal of Geodynamics*,  
760 46, 95–103, <https://doi.org/10.1016/j.jog.2008.04.005>, 2008.
- 761 Lambeck, K., Rouby, H., Purcell, A., Sun, Y., and Sambridge, M.: Sea level and global ice volumes from  
762 the Last Glacial Maximum to the Holocene, *Proceedings of the National Academy of Sciences*, 111, 15296–  
763 15303, <https://doi.org/10.1073/pnas.1411762111>, 2014.
- 764 Lambeck, K., Purcell, A., and Zhao, S.: The North American Late Wisconsin ice sheet and mantle viscosity  
765 from glacial rebound analyses, *Quaternary Science Reviews*, 158, 172–210,  
766 <https://doi.org/10.1016/j.quascirev.2016.11.033>, 2017.
- 767 Latychev, K., Mitrovica, J. X., Tromp, J., Tamisiea, M. E., Komatitsch, D., and Christara, C. C.: Glacial  
768 isostatic adjustment on 3-D Earth models: a finite-volume formulation, *Geophysical Journal International*,  
769 161, 421–444, <https://doi.org/10.1111/j.1365-246X.2005.02536.x>, 2005.
- 770 Lloyd, A. J., Wiens, D. A., Zhu, H., Tromp, J., Nyblade, A. A., Aster, R. C., Hansen, S. E., Dalziel, I. W.  
771 D., Wilson, T. J., Ivins, E. R., and O'Donnell, J. P.: Seismic Structure of the Antarctic Upper Mantle Imaged  
772 with Adjoint Tomography, *Journal of Geophysical Research: Solid Earth*, 125,  
773 <https://doi.org/10.1029/2019JB017823>, 2020.
- 774 Longman, I. M.: A Green's function for determining the deformation of the Earth under surface mass loads:  
775 2. Computations and numerical results, *Journal of Geophysical Research (1896-1977)*, 68, 485–496,  
776 <https://doi.org/10.1029/JZ068i002p00485>, 1963.
- 777 Martinec, Z.: Spectral-finite element approach to three-dimensional viscoelastic relaxation in a spherical  
778 earth, *Geophys. J. Int.*, 142, 117–141, <https://doi.org/10.1046/j.1365-246x.2000.00138.x>, 2000.
- 779 Milne, G. A., Davis, J. L., Mitrovica, J. X., Scherneck, H.-G., Johansson, J. M., Vermeer, M., and Koivula,  
780 H.: Space-Geodetic Constraints on Glacial Isostatic Adjustment in Fennoscandia, *Science*, 291, 2381–2385,  
781 <https://doi.org/10.1126/science.1057022>, 2001.
- 782 Mitrovica, J., Tamisiea, M., Davis, J., and Milne, G.: Recent mass balance of polar ice sheets inferred from  
783 patterns of global sea-level change, *NATURE*, 409, 1026–1029, <https://doi.org/10.1038/35059054>, 2001.
- 784 Mitrovica, J. X., Davis, J. L., and Shapiro, I. I.: A spectral formalism for computing three-dimensional  
785 deformations due to surface loads: 2. Present-day glacial isostatic adjustment, *Journal of Geophysical*  
786 *Research: Solid Earth*, 99, 7075–7101, <https://doi.org/10.1029/93JB03401>, 1994.
- 787 Paulson, A., Zhong, S., and Wahr, J.: Modelling post-glacial rebound with lateral viscosity variations,  
788 *Geophysical Journal International*, 163, 357–371, <https://doi.org/10.1111/j.1365-246X.2005.02645.x>,  
789 2005.
- 790 Peltier, W. R.: Postglacial variations in the level of the sea: Implications for climate dynamics and solid-  
791 Earth geophysics, *Reviews of Geophysics*, 36, 603–689, <https://doi.org/10.1029/98RG02638>, 1998.



- 792 Peltier, W. R., Argus, D. F., and Drummond, R.: Space geodesy constrains ice age terminal deglaciation:  
793 The global ICE-6G\_C (VM5a) model: Global Glacial Isostatic Adjustment, *J. Geophys. Res. Solid Earth*,  
794 120, 450–487, <https://doi.org/10.1002/2014JB011176>, 2015.
- 795 Peltier, W. R., Argus, D. F., and Drummond, R.: Comment on “An Assessment of the ICE-6G\_C (VM5a)  
796 Glacial Isostatic Adjustment Model” by Purcell et al., *Journal of Geophysical Research: Solid Earth*, 123,  
797 2019–2028, <https://doi.org/10.1002/2016JB013844>, 2018.
- 798 Qin, C., Zhong, S., and Wahr, J.: A perturbation method and its application: elastic tidal response of a  
799 laterally heterogeneous planet, *Geophysical Journal International*, 199, 631–647,  
800 <https://doi.org/10.1093/gji/ggu279>, 2014.
- 801 Ritsema, J., Deuss, A., van Heijst, H. J., and Woodhouse, J. H.: S40RTS: a degree-40 shear-velocity model  
802 for the mantle from new Rayleigh wave dispersion, teleseismic traveltimes and normal-mode splitting  
803 function measurements, *Geophysical Journal International*, 184, 1223–1236,  
804 <https://doi.org/10.1111/j.1365-246X.2010.04884.x>, 2011.
- 805 Takeuchi, H.: On the Earth tide of the compressible Earth of variable density and elasticity, *Eos*,  
806 *Transactions American Geophysical Union*, 31, 651–689, <https://doi.org/10.1029/TR031i005p00651>,  
807 1950.
- 808 Tromp, J.: Seismic wavefield imaging of Earth’s interior across scales, *Nat Rev Earth Environ*, 1, 40–53,  
809 <https://doi.org/10.1038/s43017-019-0003-8>, 2020.
- 810 Van Der Wal, W., Barnhoorn, A., Stocchi, P., Gradmann, S., Wu, P., Drury, M., and Vermeersen, B.:  
811 Glacial isostatic adjustment model with composite 3-D Earth rheology for Fennoscandia, *Geophysical*  
812 *Journal International*, 194, 61–77, <https://doi.org/10.1093/gji/ggt099>, 2013.
- 813 Wang, Y. and Li, M.: The interaction between mantle plumes and lithosphere and its surface expressions:  
814 3-D numerical modelling, *Geophysical Journal International*, 225, 906–925,  
815 <https://doi.org/10.1093/gji/ggab014>, 2021.
- 816 Wessel, P., Luis, J. F., Uieda, L., Scharroo, R., Wobbe, F., Smith, W. H. F., and Tian, D.: The Generic  
817 Mapping Tools Version 6, *Geochemistry, Geophysics, Geosystems*, 20, 5556–5564,  
818 <https://doi.org/10.1029/2019GC008515>, 2019.
- 819 Wu, P.: Using commercial finite element packages for the study of earth deformations, sea levels and the  
820 state of stress, *Geophysical Journal International*, 158, 401–408, <https://doi.org/10.1111/j.1365-246X.2004.02338.x>, 2004.
- 822 Wu, P. and Peltier, W. R.: Viscous gravitational relaxation, *Geophysical Journal International*, 70, 435–  
823 485, <https://doi.org/10.1111/j.1365-246X.1982.tb04976.x>, 1982.
- 824 Yuan, T.: Dataset for CitcomSVE 3.0: A Three-dimensional Finite Element Software Package for Modeling  
825 Load-induced Deformation for an Earth with Viscoelastic and Compressible Mantle,  
826 <https://doi.org/10.5281/zenodo.13932411>, 2024.
- 827 Zhong, S., Zuber, M. T., Moresi, L., and Gurnis, M.: Role of temperature-dependent viscosity and surface  
828 plates in spherical shell models of mantle convection, *Journal of Geophysical Research: Solid Earth*, 105,  
829 11063–11082, <https://doi.org/10.1029/2000JB900003>, 2000.



- 830 Zhong, S., Paulson, A., and Wahr, J.: Three-dimensional finite-element modelling of Earth's viscoelastic  
831 deformation: effects of lateral variations in lithospheric thickness, *Geophysical Journal International*, 155,  
832 679–695, <https://doi.org/10.1046/j.1365-246X.2003.02084.x>, 2003.
- 833 Zhong, S., Zhang, N., Li, Z., and Roberts, J.: Supercontinent cycles, true polar wander, and very long-  
834 wavelength mantle convection, *EARTH AND PLANETARY SCIENCE LETTERS*, 261, 551–564,  
835 <https://doi.org/10.1016/j.epsl.2007.07.049>, 2007.
- 836 Zhong, S., McNamara, A., Tan, E., Moresi, L., and Gurnis, M.: A benchmark study on mantle convection  
837 in a 3-D spherical shell using CitcomS, *Geochemistry, Geophysics, Geosystems*, 9,  
838 <https://doi.org/10.1029/2008GC002048>, 2008.
- 839 Zhong, S., Qin, C., Geruo, A., and Wahr, J.: Can tidal tomography be used to unravel the long-wavelength  
840 structure of the lunar interior?, *GEOPHYSICAL RESEARCH LETTERS*, 39,  
841 <https://doi.org/10.1029/2012GL052362>, 2012.
- 842 Zhong, S., Kang, K., A, G., and Qin, C.: CitcomSVE: A Three-Dimensional Finite Element Software  
843 Package for Modeling Planetary Mantle's Viscoelastic Deformation in Response to Surface and Tidal  
844 Loads, *Geochem Geophys Geosyst*, 23, <https://doi.org/10.1029/2022GC010359>, 2022.
- 845